Coastal Engineering 117 (2016) 126–137

Contents lists available at ScienceDirect

Coastal Engineering

journal homepage: www.elsevier.com/locate/coastaleng

Experimental study of uplift loads due to tsunami bore impact on a wharf model

Cheng Chen [a,b,*], Bruce W. Melville [b], N.A.K. Nandasena [b], Asaad Y. Shamseldin [b], Liam Wotherspoon [b]

[a] College of Harbor, Coastal and Offshore Engineering, Hohai University, Nanjing 210098, China
[b] Department of Civil and Environmental Engineering, The University of Auckland, Auckland 1142, New Zealand

ARTICLE INFO

Article history:
Received 27 January 2016
Received in revised form 13 June 2016
Accepted 2 August 2016
Available online xxxx

Keywords:
Tsunami bore
Uplift pressure
Wharf model
Deck
Slope

ABSTRACT

Tsunamis are unpredictable disasters that have occurred frequently in recent years. An experimental study was conducted to quantify the tsunami bore uplift loads on a deck mounted on a slope, representing a typical wharf structure. Tsunami bores were generated as dam break waves in a flume, and the bore Froude number was approximately 1.6 on the dry bed. Fifty-five tests (11 bore cases, 5 runs each cases) were conducted for detailed measurements of bore height and bore velocity, and 504 tests (7 bore cases, 3 deck heights, 8 wharf slope angles, 3 runs each combination) were conducted for measurements of time-histories of pressure on the soffit of the deck. The effects of bore height, deck height and slope angle on uplift loads were studied. Results show that bore height correlates with bore velocity. The flow motion of the tsunami bore impacting the deck is divided into five stages: front-climbing, front-hitting, run-up, quasi-steady, and recession. The uplift pressure decreases from the deck-slope connection to the deck front edge, and the total uplift load increases with increasing bore height or decreasing deck height. For the front-hitting stage (the maximum pressure), the uplift load increases as the wharf slope angle decreases. However, for the quasi-steady stage (the longest time period), the uplift load is consistent for different wharf slope angles. Based on the experimental data, the equations for predicting the front-hitting and quasi-steady pressures are proposed as functions of bore height, deck height and wharf slope angle, and the predicted values are within ±20% error.

1. Introduction

Tsunami disasters occurred frequently in the last decade and damaged coastal structures (Nandasena et al., 2012). In general, tsunami waves are faster, higher and stronger than wind waves or storm surges. Tsunami generation cannot be predicted because tsunamis are caused by the sudden displacement of significant volumes of ocean water, originally triggered by earthquakes, landslides, volcanic eruptions, or meteors (Al-Faesly et al., 2012).

On 26 December 2004, a tsunami was triggered by a 9.1 magnitude earthquake in the Indian Ocean. The maximum run-up height of the tsunami wave was 30 m, causing over 200,000 fatalities in >10 countries bordering the Indian Ocean (Grilli et al., 2007). On 27 February 2010, a tsunami was triggered by an 8.8 magnitude earthquake off the coast of Chile. The tsunami reached a localized run-up of 29 m on a coastal bluff (Fritz et al., 2011). On 11 March 2011, a 9.0 magnitude earthquake occurred near the northeast coast of Japan, and the tsunami swept along the coastline and penetrated inland with maximum run-up heights of 40 m (Yeh et al., 2013). On 16 September 2015, an 8.3 magnitude earthquake struck off the central coast of Chile, and triggered a tsunami with a maximum run-up height of 13 m (Contreras-Lopez et al., 2016).

Many port structures have been damaged by tsunamis. For example, in Thailand, dock slabs in Khao Lak port were displaced, and decks of Ban Nam Kem fishing port were severely damaged by uplift pressure due to the 2004 Indian Ocean tsunami (Ghobarah et al., 2006; Lukkunaprasit and Ruangrassamee, 2008). In Indonesia, the Banda Aceh port area was isolated and inaccessible, and the oil transfer facility of Kreung Raya port suffered extensive damage in the 2004 Indian Ocean tsunami (Ghobarah et al., 2006). In Japan, Sendai port in the Tohoku region was damaged in the 2011 Japan tsunami, and damaged containers can be clearly seen in satellite images (Suppasri et al., 2012).

In the experimental environment, a dam break flow has generally been used to simulate a tsunami bore (Nandasena and Tanaka, 2013), because the run-up motion of the tsunami bore on a dry bed is similar to that of a dam break flow (Chanson, 2006; Chanson, 2009). The analytical solution for dam break flow proposed by Chanson (2005) was compared tsunami-induced hydraulic bores that were observed during the 2004 Indian Ocean tsunami, and good agreement was observed between the analytical solution and the field data, in terms of the bore front shape. This suggests that the dam break phenomenon can be used as a method to simulate tsunami-induced hydraulic bores (Al-Faesly et al., 2012). Various simple equations have been proposed for estimating tsunami bore velocity (see, e.g., FEMA, 2012; CCH, 2000; Murty, 1977; Kirkoz, 1983; Iizuka and Matsutomi, 2000; and Bryant,

http://dx.doi.org/10.1016/j.coastaleng.2016.08.001
0378-3839/

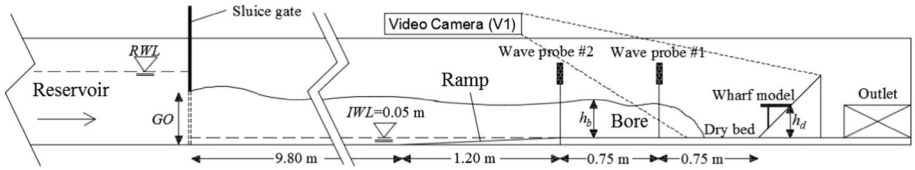

Fig. 1. Schematic of the flume.

2008), and different empirical coefficients are adopted for those equations.

Several studies have investigated tsunami wave action on individual structures such as horizontal-standing structures (deck, bridge, jetty, etc.) or vertical-standing structures (cylindrical structure, wall, etc.). For horizontal-standing structures, different characteristics of fluid forces were observed for different wave cases, i.e. in the case of broken waves, the horizontal force was stronger than the uplift force, while in the case of unbroken waves, the horizontal force was weaker than the uplift force (Kosa et al., 2010). Araki et al. (2011) investigated solitary wave forces on a bridge model and found that the fluid forces in the case of a post breaking wave were smaller than those in the case of a just breaking wave. In addition, Rahman et al. (2014) observed that a larger force was observed in a broken wave than in an unbroken wave. To quantify the wave-in-deck loads, Cuomo et al. (2007) and Kosa et al. (2010) investigated the loads on jetties and bridges, respectively. Based on their experimental data, methods were derived to predict horizontal and vertical forces. For these wave-in-deck loads, the applicability of existing prediction methods was investigated by Araki and Deguchi (2012). Further investigation of the wave-in-deck loads revealed the effect of air compression on uplift pressure due to waves (Cuomo et al., 2009; Araki, 2015), which reduces wave impact pressure and distorts the scale of the model.

For vertical-standing structures, Nouri et al. (2010) measured the pressures exerted on the upstream and lateral sides of a cylindrical structure, and found that the maximum pressure is located at 40% of the bore height. Robertson et al. (2013) carried out a series of experiments in a large wave flume to quantify tsunami bore forces on vertical walls, and found that the forces follow Froude scaling. Kihara et al. (2015) conducted large-scale experiments on the pressure exerted on a tide wall; they investigated the pressures during the bore impact, initial reflection, and quasi-steady-state phases, and found that pressures profile hydrostatically in the quasi-steady-state phase.

A few combination structures such as wall/floor systems and deck/wall structures have also been studied. Robertson et al. (2008) conducted experiments focusing on the fluid forces from a bore impacting a wall/floor system, and found that, because of the turbulent nature of the bore, there was significant variability in the impulsive uplift pressures induced on the soffit of the slab. When the bore travelled over standing water, the variability was more significant. Chock et al. (2011) conducted experiments to investigate tsunami bore actions on a deck/wall structure for many variations of slab height, wave height and still water depth, and proposed a design envelope for the uplift pressure coefficient.

Among the previous studies, a typical wharf structure (deck-slope-pile structure) has not yet been investigated. The study reported in this paper investigated the uplift loads on a wharf model subjected to a simulated tsunami bore in a flume. Section 2 describes the tsunami flume and the experimental set-up. Section 3 presents the bore characteristics and results including time-histories of uplift pressure. Section 4 compares this study with other studies and discusses the forms of the equations for estimating uplift pressure. Section 5 presents the main conclusions.

2. Experimental set-up

2.1. Tsunami bore generation

Physical model tests were carried out in a tsunami wave flume at the University of Auckland, New Zealand. The experimental facility consists of three major parts, namely a reservoir, a sluice gate and a flume (Fig. 1). The reservoir covers an area of 77 m^2, with a capacity for storing water of approximately 50 m^3. The reservoir water level (*RWL*) can reach a maximum height of 0.6 m. The flume is 14 m long, 1.2 m wide and 0.8 m high. The reservoir and the flume are connected by a steel sluice gate, which is 1.2 m wide and 0.6 m height. The sluice gate consists of two individual gates, a sliding gate and a shutter gate. The sudden lifting of the sliding gate and the simultaneous opening of the shutter gate were both controlled by a computer. The rising speed of the sliding gate was 0.65 m/s, giving lifting times of 0.31 s, 0.46 s, and 0.62 s for gate opening heights (*GO*) of 0.2 m, 0.3 m and 0.4 m, respectively. The tsunami bores were generated by the release of the water from the reservoir into the flume. Preliminary tests showed that it requires at least 3 s of gate open time to make bores fully developed. So the sliding gate was kept open at the required *GO* for 4 s, which is long enough to generate stable bores. The resulting bore length can be considered long enough when compared with the flume length. In the flume, the initial water level (*IWL*) was 0.05 m in all experiments, to simulate the foreshore area. In the case of a propagating tsunami wave, a trough can arrive first, in which case a drawback of sea water will occur and the seabed will be exposed to the air. To simulate this dry bed condition, the elevation of the flume bed was increased by 0.05 m for 1.5 m upstream of the toe of the wharf slope. A 1.2 m long ramp was installed upstream of the dry bed section to simulate a shore condition which gradually changed from wet- to dry-bed. A drain channel with an outlet was provided behind the slope for quick draining after each test.

2.2. Wharf model

Fig. 2(a) shows the side view of the wharf model. An adjustable slope was installed near the end of the flume, and across the full flume width. A horizontal deck was mounted on the slope and supported by six steel piles. The deck and slope were made of plexiglass with thickness of 15 mm. A steel frame was fixed to the slope to provide enough rigidity. The angle of the wharf slope (θ) was adjustable, as was

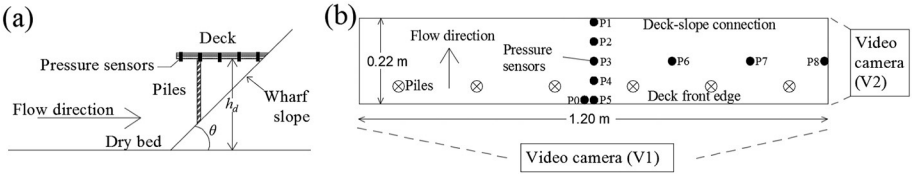

Fig. 2. Schematic of the wharf model: (a) the side view of the wharf model; (b) the plan view of the deck.

Table 1
Summary of bore measurements.

Bore case	*RWL* (m)	*GO* (m)	h_b (min, max) (m)	u_b (min, max) (m/s)
1	0.3	0.2	0.15 (0.14, 0.16)	1.68 (1.59, 1.71)
2	0.3	0.3	0.15 (0.15, 0.15)	1.93 (1.91, 1.96)
3	0.4	0.2	0.17 (0.16, 0.19)	2.04 (1.97, 2.07)
4	0.4	0.3	0.19 (0.18, 0.20)	2.12 (2.11, 2.14)
5	0.4	0.4	0.20 (0.19, 0.20)	2.25 (2.23, 2.26)
6	0.5	0.2	0.21 (0.20, 0.22)	2.24 (2.09, 2.33)
7	0.5	0.3	0.25 (0.25, 0.25)	2.53 (2.44, 2.65)
8	0.5	0.4	0.25 (0.23, 0.26)	2.46 (2.36, 2.58)
9	0.6	0.2	0.22 (0.21, 0.23)	2.34 (2.20, 2.51)
10	0.6	0.3	0.27 (0.27, 0.27)	2.71 (2.67, 2.76)
11	0.6	0.4	0.28 (0.27, 0.28)	2.61 (2.50, 2.73)

Note: each bore case was measured five times. *RWL* — reservoir water level; *GO* — gate opening; h_b (min, max) — averaged (maximum, minimum) bore height at wave probe #2; u_b (min, max) — averaged (maximum, minimum) bore velocity between wave probes #1 and #2.

the height of the deck above the dry bed (h_d). The length of the piles was changed accordingly to keep the deck horizontal.

Fig. 2(b) is the plan view of the deck. The wharf model was 1.2 m wide, and across the full width of the flume to achieve a quasi-two dimensional experiment. The deck length in the stream-wise direction was 0.22 m. Eight pressure sensors (Honeywell S&C 26PCBFA6D) were attached to the soffit of the deck to capture the pressure time-histories. Five of them (P1, P2, P3, P4, P5) were evenly distributed along the centreline of the deck in the stream-wise direction, and four of them (P3, P6, P7, P8) were used to investigate the pressure variation in the transverse direction. The pressure sensors are wet-wet differential sensors that can measure negative or positive pressure with a range of ±34.5 kPa, and at a frequency of 1000 Hz. The side-view of the wharf model is visible through a glass window in the side of the flume. High-speed camera recordings (Casio Exilim EX-FH 20, 210 frames per second) were used to investigate the flow motion around the wharf model, both from the front view (V1) and the side view (V2).

2.3. Experimental conditions

For bore measurements, 55 tests were conducted, i.e. 11 bore cases (Table 1), varied by changing the combinations of gate opening and reservoir water level, and 5 repetitive runs for each bore case. For pressure measurements, the wave probes were removed from the flume to eliminate their effects on flow, and 504 tests were conducted. Seven bore cases (1, 3, 4, 6, 8, 9, and 11) were selected from the previous bore measurements, for each bore case there were 3 deck heights (h_d = 0.20, 0.25, and 0.30 m), for each deck height there were 8 wharf slope angles (θ = 20, 25, 30, 35, 40, 45, 50, and 90°), and there were 3 repetitive runs for each combination (bore case + deck height + wharf slope angle).

2.4. Data processing procedures

2.4.1. Incident bore heights

The time-histories of water level from wave probes were recorded. In each test, the bore height (or inundation depth) was taken as the height when the recorded water level stabilized for the first time. The bore height was taken from wave probe #2 rather than wave probe #1 (Fig. 1), because wave probe #1 received the reflected wave from the wharf model before the water level stabilized.

2.4.2. Incident bore velocities

To quantify incident bore velocities in front of the wharf model, two techniques were explored in this study: 1) data from two wave probes (#1 and #2 in Fig. 1) installed at 0.75 m and 1.5 m in front of the wharf slope toe, respectively; 2) high-speed camera recordings that were used to roughly double check the accuracy of the measured velocities. The bore velocities were estimated using the spacing between two wave probes of 0.75 m and the time required for the tsunami bore to travel between the two wave probes. In this study, the bore was assumed to pass the wave probe when the water level in the wave probe recording rose to 50 mm.

2.4.3. Uplift pressures

The time-histories of pressure were recorded by eight pressure sensors (Fig. 2(b)). Due to the unavoidable vibrations of the wharf model and pressure sensors' tubes, vibration noise contaminated the pressure signals (Fig. 3). To investigate the vibration noise, in a preliminary test another pressure sensor (the same as other pressure sensors) was mounted at P0 (Fig. 2(b), 10 mm away from P5). The nozzle attached to the soffit of the deck was totally blocked, and therefore only vibration noise was recorded rather than contaminated pressure signals. Results of the preliminary test showed that the magnitude of the positive and negative vibration noise is equal. The vibration noise was greatly reduced by using the following filtering procedure, which allowed the extraction of the pressure signals from the originally contaminated signals:

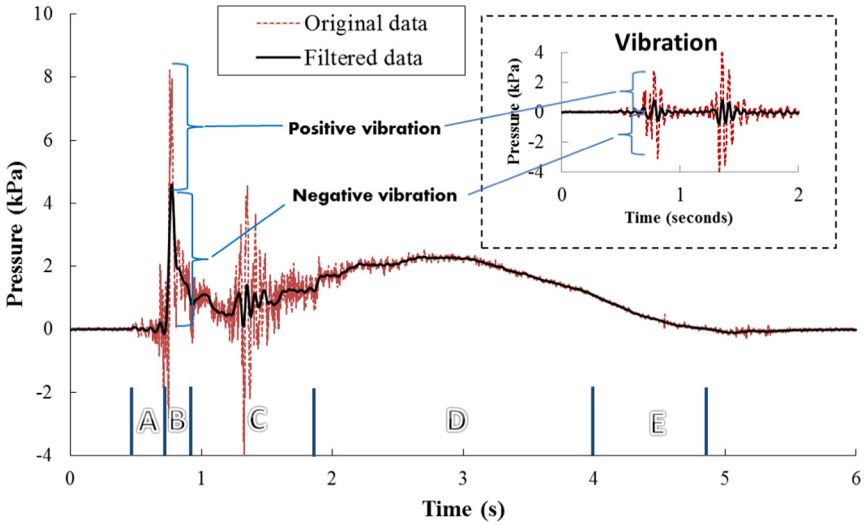

Fig. 3. Time-history of pressure at P5 (bore case = 11 in Table 1, h_d = 0.30 m, θ = 30°).

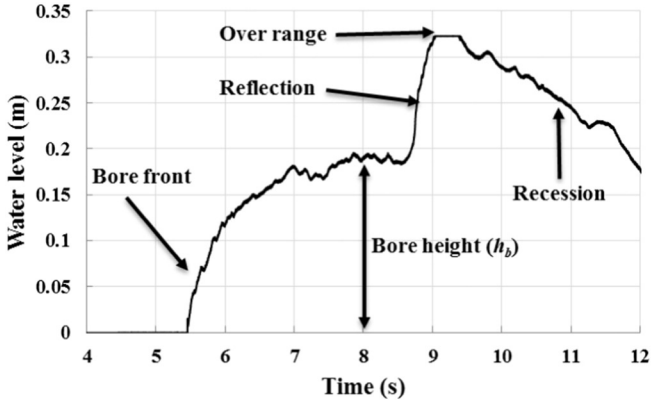

Fig. 4. Water level recorded by wave probe #2 (bore case = 4 in Table 1).

- The vibration noise from P0 (Fig. 2(b)) was recorded (inset in Fig. 3).
- The record was analysed to find the main period of the vibration noise, T.
- The main period of the vibration noise was confirmed to be short-term fluctuations compared with the original pressure signals.
- Obtained the filtered pressure signals as $p(t) = \frac{1}{T}\int_{t-0.5T}^{t+0.5T} p_o(t)$, where t is the time, $p_o(t)$ is the original pressure at t, and $p(t)$ is the filtered pressure at t.

3. Results

3.1. Tsunami bore

3.1.1. Bore heights and velocities in front of wharf model

Fig. 4 shows the time-history of the water level (bore surface) for bore case = 4 (see Table 1). The initial time ($t = 0$ s) denotes the sluice gate opening. The shape of the bore front is also indicated by the water level variation with time in Fig. 4. The sloping front of the bore reached the wave probe at 5.4 s, after which the water level rose rapidly and stabilized at 0.19 m, at about 8.0 s. This stabilized value is taken as the bore height (h_b) in this study. At 8.7 s, the water level rose again because of the wave reflected by the wharf model. Water levels above 0.33 m were out of the range of the wave probe. Finally, after 9.4 s the water level dropped down because the flow receded.

Details of measurements of tsunami bore height and bore velocity in front of the wharf model are listed in Table 1. As expected, bore height (h_b) increased with increasing reservoir water level (RWL) or increasing gate opening (GO), and the velocity correlates with the bore height. In this study, the bore Froude number (Fr_b) in front of the wharf model is defined as the relationship between bore height and bore velocity:

$$Fr_b = u_b/\sqrt{gh_b} \tag{1}$$

where, u_b is bore velocity and g is the gravitational acceleration.

The Fr_b greatly depends on the upstream conditions near the position of interest, e.g. bed friction, initial water depth, shore slope angle, and obstacles. For example, in this study, Fr_b varied from 1.4 to 1.7 for waves travelling on a 2.4° ramp upstream of a dry bed in the flume (for h_b = 0.15 to 0.28 m). Fr_b values from other studies bracket the values from this study: Fr_b varied from 2.4 to 3.0 for waves travelling on a slope of 0.5° (Lukkunaprasit et al., 2009); Fr_b ranged from 0.7 to 2.0 for the Sumatra tsunami in Thailand and Indonesia (Matsutomi et al., 2006); and Fr_b of the 2011 Japan tsunami varied from 1.14 to 1.5 (Nandasena et al., 2012). The coefficient value adopted in a particular velocity formula is actually the average Fr_b value for that position of interest, and a wide range of coefficients has been proposed, such as 2.0 by FEMA (2012), 1.83 by Murty (1977), 1.41 by Kirkoz (1983), and 1.1 by Iizuka and Matsutomi (2000). As a result, there is no general formula for velocity because its coefficient depends on characteristics of the area of interest. The average coefficient is approximately 1.6 in this study, which is between those in the Murty and Kirkoz formulas.

3.1.2. Flow motion around the wharf model

Different flow motions were observed in the different stages of the tsunami bore hitting the wharf model (see A to E in Fig. 3). In the first stage, the front-climbing stage (A), the tsunami bore front was climbing up the slope, and about to hit the deck. For the fully developed bore, the

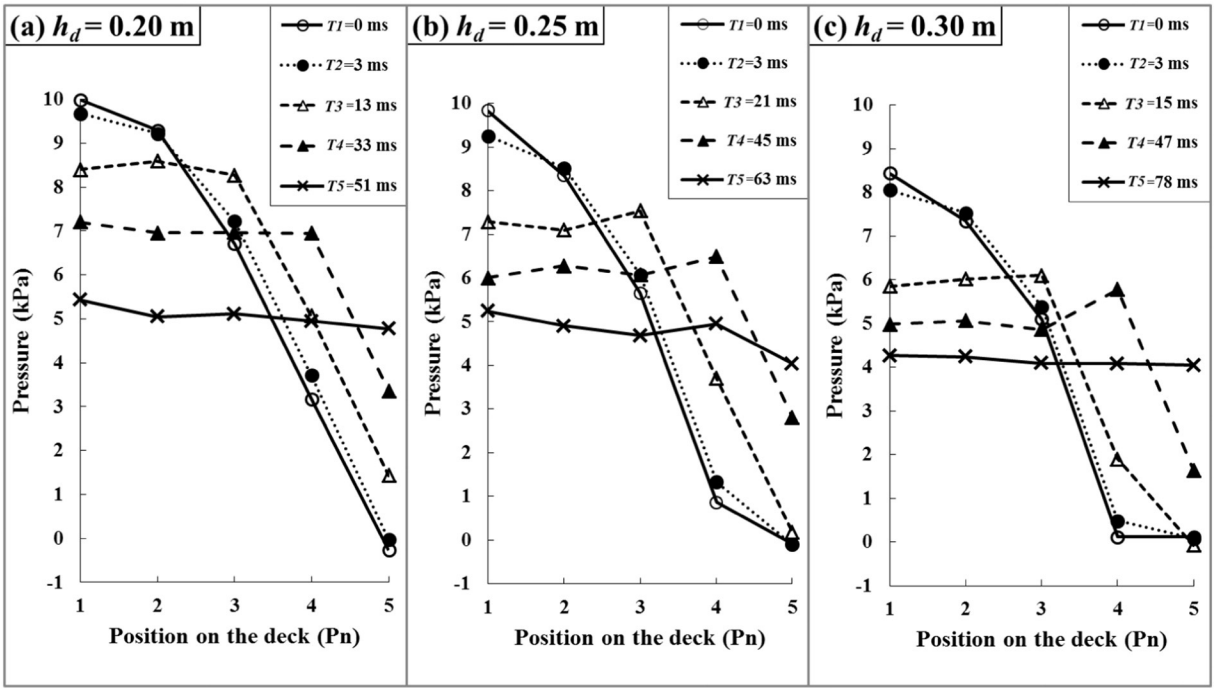

Fig. 5. Pressure distribution along stream-wise centreline in front-hitting stage (bore case = 11 in Table 1, and $\theta = 30°$).

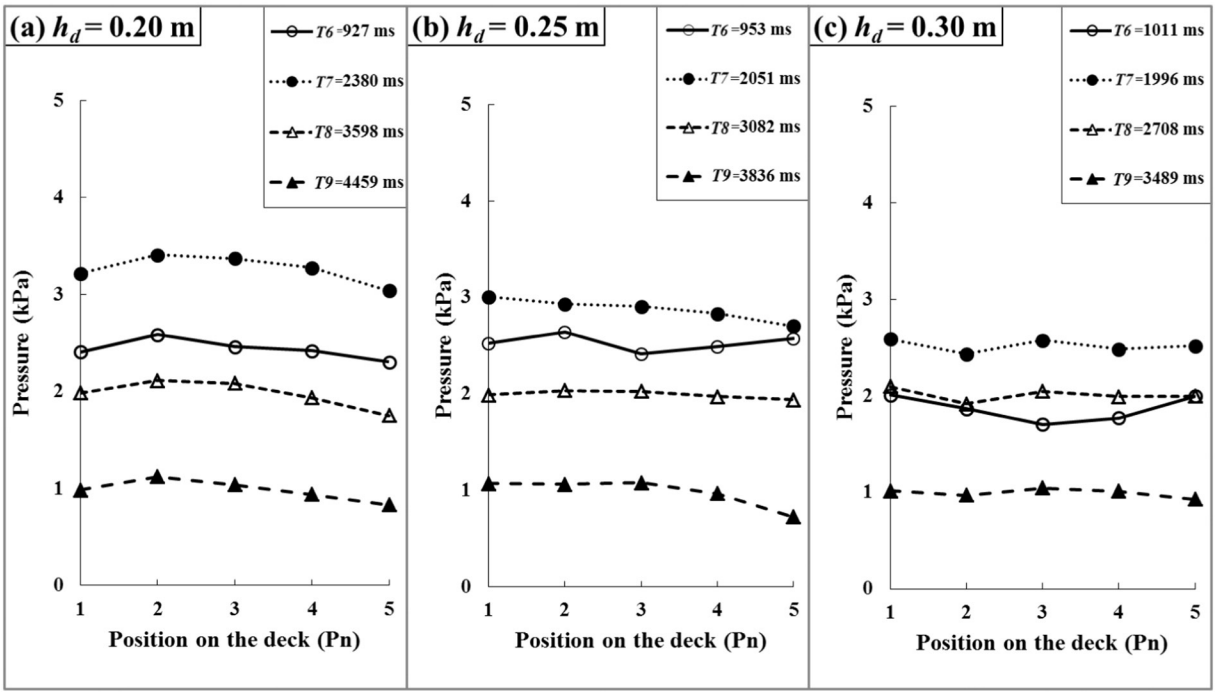

Fig. 6. Pressure distribution along stream-wise centreline in quasi-steady stage (bore case = 11 in Table 1, and $\theta = 30°$).

run-up water line forms distinct scallops in plan, and this is similar to the observations of Yeh et al. (1989). Yeh et al. (1989)'s study suggested that the irregular water line results partly from the effect of the sidewalls, and this effect cannot be eliminated in the laboratory environment. In the second stage, the front-hitting stage (B), the bore front hit the deck, and the flow appeared like a tongue of water slapping the soffit of the deck with strong force. In the third stage, the run-up stage (C), the bore front dropped down due to gravity and blocking by the deck, and encountered the upcoming flow and filled the underdeck space with turbulence flow and air bubbles in this 2-D flume environment. At this stage, the water level in front of the deck increased and fluctuated. The fluctuation was caused by the interaction between the reflected bore front and the upcoming bore body. In the fourth stage, the quasi-steady stage (D), the main body of the bore overcame the reflected bore front and engulfed the wharf. The water completely inundated the deck, the water level in front of the deck stopped rising, and thus became quasi-steady. In the final stage, the recession stage (E), the bore receded because the sluice gate was closed and the drain gate was opened.

3.2. Uplift pressure

3.2.1. Time-history of the pressures

Fig. 3 shows the time-history of the pressure at P5 (Fig. 2(b)) for bore case = 11 (Table 1), h_d = 0.30 m, and $\theta = 30°$. The dash line shows the original data and the solid line shows filtered data. The filtering procedure removed >85% noise from the original signals. The time-history of the pressure exerted on the soffit of the deck can be divided into five stages, corresponding to the five stages of the bore hitting the wharf described above (A to E in Fig. 3). Stage A is the front-climbing pressure, which is 0.3 to 0.4 s before tsunami bore impact on the deck. Before actual impact on the deck, some slight fluctuations were observed in the recorded time-history of the pressure. These fluctuations occurred when the bore front was climbing the slope, because the pressure sensors can detect the slight vibrations caused by the bore impact on this deck-slope structure (signals were not directly due to water). Stage B is the front-hitting pressure (p_f), when the bore front was impinging on the soffit of the deck. This pressure is dominated by the

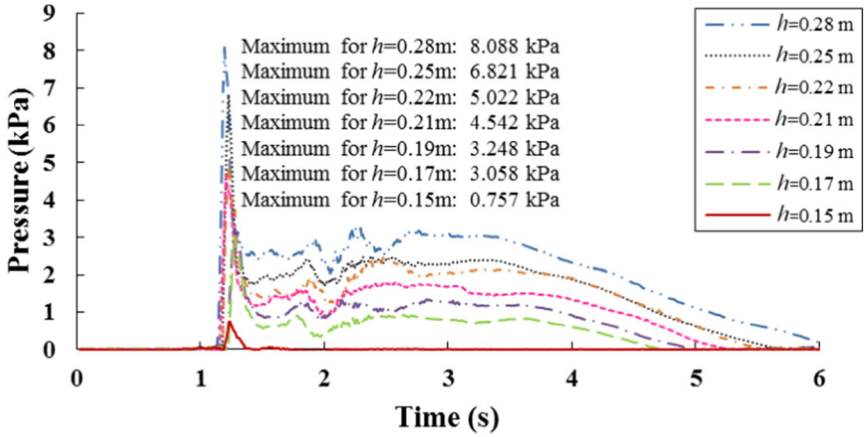

Fig. 7. Uplift pressure at deck midpoint for bore heights (h_b) (h_d = 0.25 m and $\theta = 35°$).

dynamic pressure due to bore front impact, because the inundation water level was lower than the soffit of the deck in this stage. This pressure increased rapidly to a peak with an immediate decrease. Stage C is the run-up pressure, when the pressure was characterized by large fluctuations. These strong fluctuations occurred when the upcoming bore body encountered the reflected bore front. The fluctuations varied with model configuration and bore height. Meanwhile, the pressure increased gradually after the bore front was reflected, and the upcoming flow kept on hitting the deck. Stage D is the quasi-steady pressure (p_q), because the pressure appeared quasi-steady when the tsunami flow became quasi-steady and the inundation height reached its maximum. This quasi-steady pressure is dominated by hydrostatic pressure, because the maximum inundation water level is about 0.2 m higher than deck soffit (although the water level was fluctuating). Stage E is the recession pressure, because the tsunami receded and the pressure eventually dropped to zero.

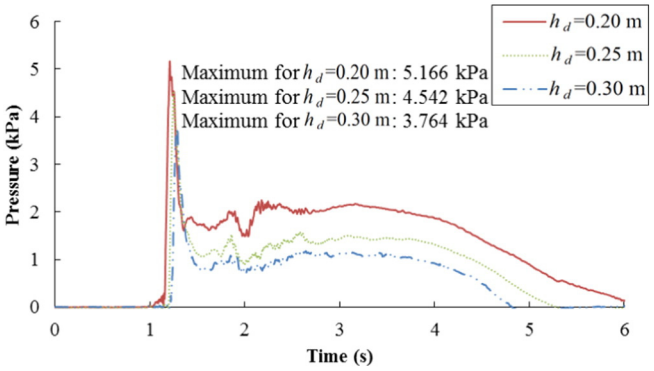

Fig. 8. Uplift pressure at deck midpoint for deck heights (h_d) (bore case = 6 in Table 1 and $\theta = 35°$).

3.2.2. Pressure profile variation in the front-hitting stage

In the front-hitting stage, pressure distribution along the deck centreline in the stream-wise direction varied significantly because the bore front hit different deck positions over a short time, and this pressure was dominated by the dynamic pressure. Fig. 5 shows pressure variation along stream-wise centreline in the front-hitting stage for bore case = 11 (Table 1) and $\theta = 30°$. The horizontal axis is the position on the deck (P1–P5 in Fig. 2(b)) and the vertical axis is the pressure. $T1$–$T5$ denote the time of the recorded peak pressure (peak time) at P1–P5, respectively. The bore front hit the deck-slope connection (P1) first, and then hit P2 to P5 successively. For $T1 = 0$ ms, the pressure at P1 reached its maximum value while the pressure at P5 was still zero, indicating there is a lag in time for different positions to received maximum pressure. The difference between the peak times for P1 and P2 ($T1$ and $T2$) is 3 ms and the same for all deck heights, but the interval time between $T1$ and $T5$ increases with increasing deck height (h_d), from 51 ms to 78 ms. This is because the velocity head of the bore front was smaller when it hit a higher deck. For $T5$, the pressure distribution along the stream-wise centreline of the deck became almost constant because it is coming into the run-up stage. For all the deck heights, the deck was exposed to the maximum average pressure (6.9 kPa for $h_d = 0.20$ m, 5.8 kPa for $h_d = 0.25$ m, and 4.8 kPa for $h_d = 0.30$ m) when the pressure at P4 reached its maximum (at $T4$).

3.2.3. Pressure profile variation in the quasi-steady stage

Fig. 6 shows pressure variation along the stream-wise direction in the quasi-steady stage for bore case = 11 (Table 1) and $\theta = 30$. $T6$ denotes the start time of the quasi-steady stage, $T7$ denotes the time when deck-averaged pressure reached its maximum, and $T8$ and $T9$ denote the time when the deck-averaged pressure dropped down to 2 kPa and 1 kPa, respectively. The quasi-steady stage started earlier for a lower deck than for a higher deck. Also, a lower deck experienced a longer quasi-steady stage than a higher deck. In contrast with the front-hitting pressure, these pressure profiles along the stream-wise deck centreline are close to horizontal, indicating that the quasi-steady pressure is dominated by hydrostatic pressure.

3.2.4. Pressure distribution patterns on deck

For analysis of pressure distribution patterns on the soffit of the deck, the front-hitting pressures are analysed because they are the maximum pressures; the quasi-steady pressures are also analysed because they are the second largest pressures during the time-history and they occur for the longest time. For the front-hitting pressure distribution along the stream-wise centreline, the pressure gradually decreases from the deck-slope connection to the deck front edge. For the quasi-steady pressure distribution along the stream-wise centreline, the pressure decrease from the deck-slope connection to the deck front edge tends to be linear. For the front-hitting pressure distribution along the transverse centreline, the pressure values were relatively consistent over most of the deck (P3, P6, and P7), and the differences are <10% of mean. However, at the side of the deck (P8) the pressure drops to about half of mean. The possible reasons for the side effect are: 1) there was a 10 mm gap between the slope-deck model and the flume side, allowing dissipation of part of front-hitting energy; 2) the walls of the flume were made of bricks, and the roughness of the bricks reduced the energy of the near-wall tsunami bore. For the quasi-steady pressure distribution along the transverse centreline, the pressure values are relatively consistent for the whole deck. It can be concluded that the data captured along the stream-wise centreline are reliable and can represent the overall uplift pressure on the deck, and the side effect for the front-hitting pressure can be neglected in the following analysis.

3.3. Effect of bore height, deck height and wharf slope angle on pressures

3.3.1. Uplift pressures for different bore heights

The bore height effect on uplift pressures was investigated for seven selected cases (1, 3, 4, 6, 8, 9, and 11 in Table 1), with bore height ranging from 0.15 m to 0.28 m. Fig. 7 shows the time-histories of uplift pressure that was measured at the deck midpoint (P3) for $h_d = 0.25$ m and $\theta = 35°$. The time-histories have similar shapes and exhibit front-hitting pressure, run-up pressure and quasi-steady pressure, and eventually drop to 0 kPa. The uplift pressure increases with increasing bore height. In this study, the front-hitting pressure is two to three times the quasi-steady pressure. With increasing bore height, the increase in front-hitting pressure was greater than the increase in the quasi-steady pressure. The reason is that the front-hitting pressure is the dynamic pressure due to the impact of the bore front but the quasi-steady pressure is the hydrostatic pressure, so the dynamical mechanism for the formation of the two types of pressure is different. However, the changing rate of the maximum pressure at the front-hitting stage among cases with

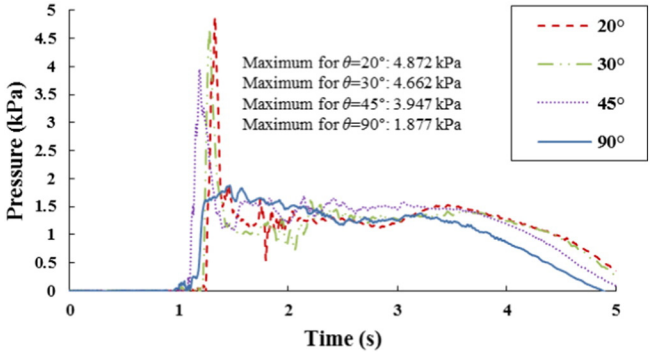

Fig. 9. Uplift pressure at deck midpoint for wharf slope angles (θ) (bore case = 6 in Table 1 and $h_d = 0.25$ m).

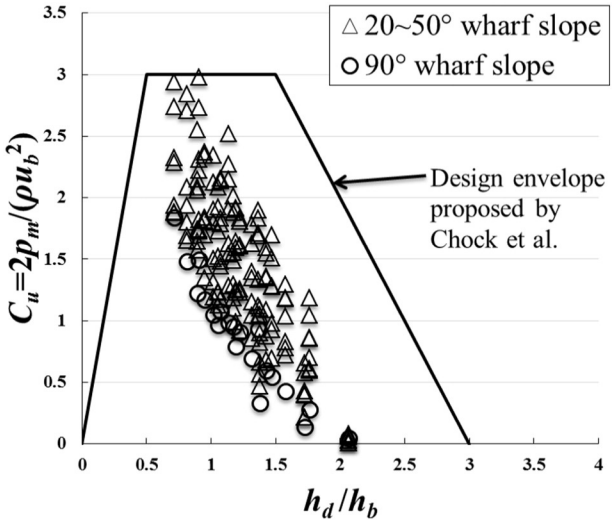

Fig. 10. Uplift pressure coefficients for dry-bed data.

different bore height would be approximately the same as that of the maximum pressure at the quasi-steady stage among cases with different bore height. This is because both the dynamic pressure and hydrostatic pressure depend on the water head. Note that, for the 0.15 m bore height (bore case = 1), the front-hitting pressure is 0.8 kPa, and the quasi-steady pressure is 0 kPa. That means the bore front touched the deck, and then the bore body was too weak to climb up the slope and exert pressure on the deck.

3.3.2. Uplift pressures for different deck heights

The deck height effect on the uplift pressures was investigated for three deck heights (h_d = 0.20, 0.25, and 0.30 m). Fig. 8 shows the time-histories of pressure at the deck midpoint (P3) for bore case = 6 (Table 1) and $\theta = 35°$. As expected, a lower deck height results in a higher pressure, both in the front-hitting stage and the quasi-steady stage. The maximum pressure decreased from 5.2 kPa to 3.8 kPa when the deck height increased from 0.20 m to 0.30 m. Note that the time of the peak lagged for the higher deck, because it took longer time for the bore front to climb up the slope and reach the higher deck.

3.3.3. Uplift pressures for different wharf slope angles

The wharf slope angle effect on the uplift pressures was investigated for eight slope angles (θ = 20, 25, 30, 35, 40, 45, 50, and 90°). Fig. 9 shows the time-histories of pressure at deck midpoint (P3) for bore case = 6 (Table 1), h_d = 0.25 m, and for four wharf slope angles. With the increasing wharf slope angle, the front-hitting pressure decreases, but there is no distinct change in the run-up pressure or the quasi-steady pressure. Specifically, the front-hitting pressure decreased from 4.9 kPa to 3.9 kPa as the wharf slope angle increased from 20° to 45°. However, the run-up pressures and quasi-steady pressures for all angles varied between approximately 0.6 to 1.8 kPa. For the 90° wharf slope angle (i.e., a vertical wall), most of the bore front was reflected. As a result, a front-hitting pressure was not observed at the deck midpoint (P3) for this special slope angle. However, it was still observed at the deck-slope connection (P1). As the wharf slope angle decreased, there was an increasing lag in time to peak pressure, because the smaller wharf slope angle resulted in longer slope length (with deck height constant), and a longer time for the tsunami bore to climb up the longer slope and hit the soffit of the deck.

4. Discussion

4.1. Data comparisons

4.1.1. Comparison of maximum uplift loads between dry bed and wet bed

Considering the 90° wharf slope angle in this study, Chock et al. (2011) carried out a tsunami bore experiment on a similar structure installed on a wet bed. Our experimental results and the design envelope that Chock et al. (2011) proposed are plotted in Fig. 10. The horizontal axis is the deck height relative to the bore height (h_d/h_b), and the vertical axis is the coefficient (C_u) for the maximum uplift force, which is expressed as:

$$C_u = 2p_m/(\rho u_b^2) \tag{2}$$

where C_u is the hydrodynamic uplift coefficient, p_m is the maximum deck-averaged uplift pressure, ρ is the density of water.

Our dry-bed data for $\theta = 90°$ inhabit the dense area of Chock et al.'s plot. The data for the dry-bed condition are more centralized than those for the wet-bed condition in the study by Chock et al., but this may due to the experimental range. The initial still water does have an effect on uplift loads, and significant uplift pressure variability was shown when the bore travelled over standing water. All the dry-bed data are within the design envelope, and this means that, for our experimental range, the use of the design envelope proposed by Chock et al. for the wet-bed condition can be extended to the dry-bed condition. However,

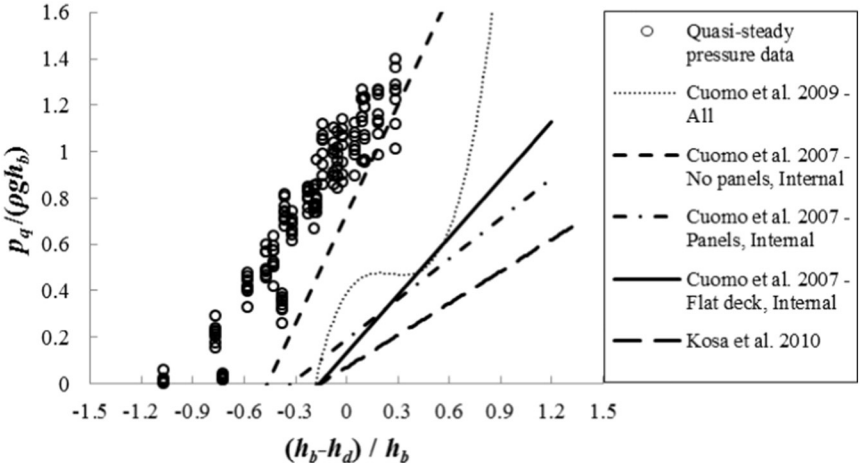

Fig. 11. Comparison of wave-in-deck and bore-in-deck quasi-steady pressure.

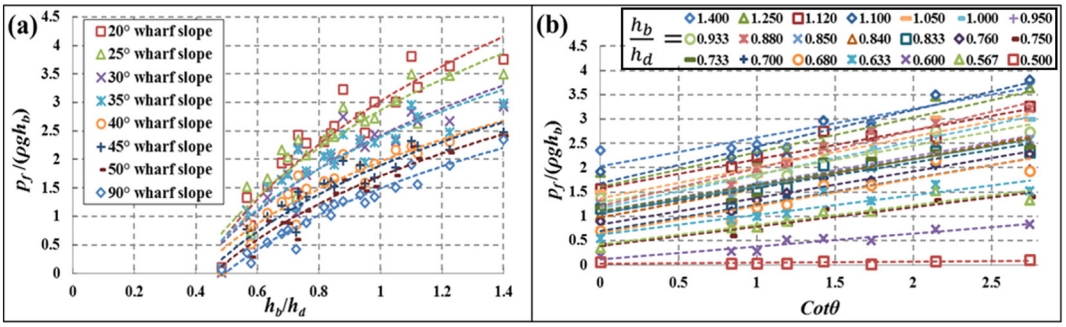

Fig. 12. Relationship between normalized front-hitting pressure and the parameters in Eq. (4).

the deck length and the bore Froude number will have an effect on the deck-averaged uplift pressure, and these variables should be investigated in future work.

4.1.2. Comparison of wave-in-deck and bore-in-deck quasi-steady pressure

Early studies investigated wave-in-deck loads (e.g., Cuomo et al., 2007; Cuomo et al., 2009; Kosa et al., 2010). These studies were performed using decks that suspended above the still water level (swl). The idealised time-history of wave-in-deck load consists of a short duration pulse, a positive quasi-steady component, and a negative quasi-static component. The quasi-static duration is of the order of magnitude of the wave period. Thus, the positive quasi-static pressure has a mechanism similar to that of the quasi-steady pressure (p_q) in this study. Despite the different wave conditions, their positive quasi-static equations from wave-in-deck tests are compared with our data in Fig. 11, based on the following assumptions:

- The wave crest above the swl is assumed to be the bore height (h_b).
- The deck clearance above the swl is assumed to be the deck height (h_d).
- The initial water depth is assumed to be the bore height (h_b).
- The incident significant wave height is assumed to be the bore height (h_b).

As Fig. 11 shows, the bore-in-deck loads are larger than wave-in-deck loads for the same normalized height of $(h_b-h_d)/h_b$. It should be noted that, for $-1<(h_b-h_d)/h_b<0$, the bore-in-deck loads are still significant because the deck was mounted on a slope rather than suspending above the water, thus the bore can climb up the slope to hit the deck. For $0<(h_b-h_d)/h_b<0.3$, the prediction equation proposed by Cuomo et al. (2007) for wave-in-deck loads on internal elements of a deck (no panels) is close to the bore-in-deck loads in this study.

Early studies of wave-in-deck loads also show the effect of air compression on uplift pressure due to waves (Cuomo et al., 2007; Cuomo et al., 2009; Araki, 2015). An air pocket trapped within a chamber beneath the deck reduces the wave impact pressure and distorts the scale of the model. In Araki (2015)'s study, the air compression effect for the broken wave is less than those for the non-breaking and just breaking wave.

In this study, the air compression is not compared to their wave-in-deck model (Cuomo et al., 2007; Cuomo et al., 2009; Araki, 2015) for the following reasons:

- The soffit of the deck was flat (without beams), so there was no chamber to trap an air pocket.
- Ephemeral forces were hard to observe in such a small scaled model.
- The bore was a broken wave, and air beneath the deck could escape through the broken bore front.
- No air pocket was observed under the soffit of the deck in the high-speed camera recordings from the side view (V2 in Fig. 2(b)).

Although air compression was not significant in this study, it is still an important issue on bore-in-deck loads. Future work could investigate the air compression effect by adding beams under the deck to form chambers.

4.1.3. Scale effects on predicted forces on prototype

A tsunami bore is free surface gravity flow. The study by Robertson et al. (2013) confirmed that Froude scaling is appropriate for tsunami bore forces on a solid wall. In this study, based on the assumption of 5 m bore height during a real tsunami and the median value of the experimental bore height (0.2 m), a geometrical similarity scale of 1:25 was adopted. For wave-impact loads on deck, Cuomo et al. (2009) suggested that the "compression law" for the role of air can also be used to gain insights on scale effects, thus the Froude scaling was found to overestimate the impact pressure. Cuomo et al. (2009) also suggested that scale affects the reduction effectiveness of impact pressure due to deck openings, and that the pressure on the deck will be much lower than that predicted using Froude scaling. From the study by Cuomo et al. (2009), it can be seen that the scale effect on bore-impact loads should also be investigated in the future work, especially for the decks with beams (where the air compression could be significant).

In addition, the slope in this experiment was plexiglass, while in a prototype the slope is composed of armour rock for slope protection, which will reduce the energy of the bore. For this reason as well, the uplift pressure on the deck in prototype will be lower than those scaled from the experimental environment.

4.2. Quantifying tsunami loads

4.2.1. Dimensionless analysis of uplift loads

The front-hitting pressure exhibits a large peak over a short period of time, so it tends to cause localized damage such as to individual deck slabs or joint connections by crushing. However, the quasi-steady pressure is generally the second largest pressure and has the longest duration, so it leads to overall failure such as sliding, shearing failure or foundation scouring. Hence, both front-hitting pressure and quasi-steady pressure are quantified herein.

The main parameters that determine the uplift pressure on the deck are:

$$p = f(\rho, g, h_b, u_b, a, h_d, \theta) \tag{3}$$

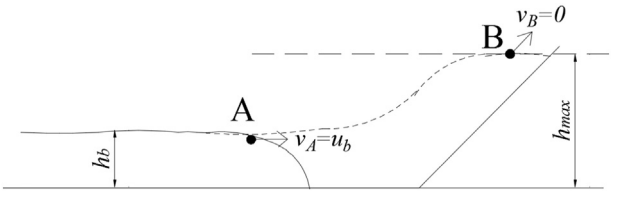

Fig. 13. Bore front climbing up to the maximum height without blocking by deck.

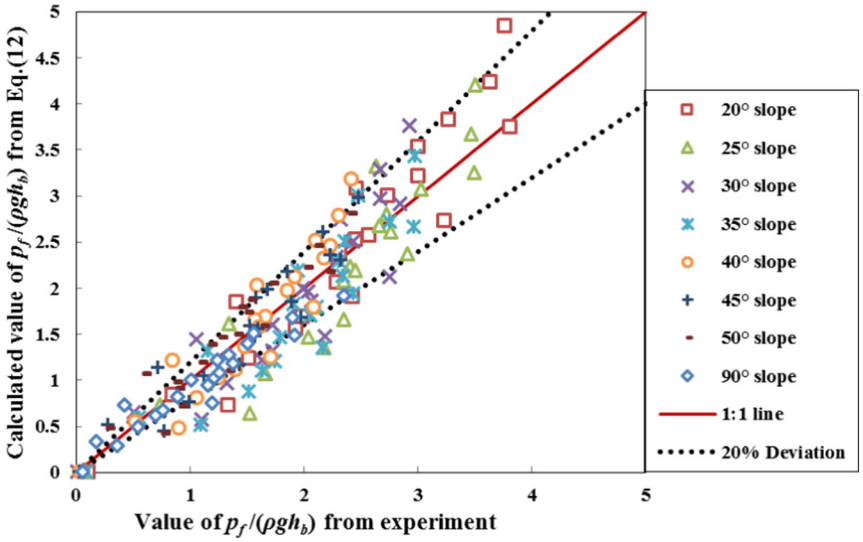

Fig. 14. Comparison of values of normalized front-hitting pressure from Eq. (12) and from experiment.

where p is deck-averaged uplift pressure and a is deck width in the stream-wise direction. Eq. (3) includes a consideration of water properties (ρ, g), the approach bore characteristics (h_b, u_b), and wharf structure geometry (a, h_d, θ).

In this study, the water properties and deck width (a) have been constant, so they can be eliminated from dimensionless analysis. Because the pressure increases with the increasing bore height (h_b) or the decreasing deck height (h_d), the ratio of bore height to deck height (h_b/h_d) was used as the dimensionless height parameter. The quasi-steady pressure is dominated by hydrostatic pressure, so it is normalized by $(\rho g h_b)$. The front-hitting pressure is dynamic pressure and should be normalized by (ρu_b^2). From Eq. (1), $\rho u_b^2 = Fr_b^2 \rho g h_b$, and (Fr_b) is 1.6 in this study, so the front-hitting pressure can also be normalized by $(\rho g h_b)$. Thus, Eq. (3) can be written in non-dimensional form as:

$$\frac{p}{\rho g h_b} = f\left(Fr_b, \frac{h_b}{h_d}, cot\theta\right) \tag{4}$$

In this study, the average bore Froude number (Fr_b) is 1.6, and the ranges for the dimensionless parameters in Eq. (4) are: $0.5 \le h_b/h_d \le 1.4$, and $0 \le \cot\theta \le 2.75$, respectively.

4.2.2. Equation for estimating front-hitting pressures

Fig. 12(a) and (b) show the relationship between the normalized front-hitting pressure and the height and wharf slope parameters in Eq. (4), respectively. In general, the normalized pressure increases with increasing h_b, and decreases with increasing h_d, but the data are scattered. However, as seen from Fig. 12(a), a correlation exists between the normalized front-hitting pressure and dimensionless parameter (h_b/h_d), expressed as Eq. (5). As seen from Fig. 12(b), a linear relationship exists between the normalized front-hitting pressure and the dimensionless parameter $(\cot\theta)$, expressed as Eq. (6).

$$\frac{p_f}{\rho g h_b} = f(\theta) * \ln\left(\frac{h_b}{h_d} * C_1\right) \tag{5}$$

$$\frac{p_f}{\rho g h_b} = (\cot\theta + C_2) * f\left(\frac{h_b}{h_d}\right) \tag{6}$$

where p_f is the maximum deck-averaged front-hitting pressure, C_2 is the coefficient with respect to the vertical wall effect (for a vertical wall, $\theta = 90°$, and $(\cot\theta + C_2) = C_2$); C_1 is the coefficient with respect to energy loss as the bore front climbs the wharf slope, which will be discussed below.

From Eqs. (5) and (6), the following numerical form is obtained:

$$\frac{p_f}{\rho g h_b} = (\cot\theta + C_2) * \ln\left[\frac{h_b}{h_d} * C_1\right] \tag{7}$$

As seen from the experimental data in Fig. 12(a), for all wharf slope angles, when $h_b/h_d = 0.5$, $p_f/(\rho g h_b) \approx 0$, therefore $C_1 = h_d/h_b = 2$, to satisfy Eq. (7).

Considering the basic theory, when unit water volume of the bore front at A climbs to the maximum height B (Fig. 13), the law of conservation of energy can be applied (neglecting temporal variations):

$$\rho g h_{max} + \frac{1}{2}\rho u_B^2 = \rho g h_b + \frac{1}{2}\rho u_A^2 - \frac{1}{2}k_1 \rho u_A^2 \tag{8}$$

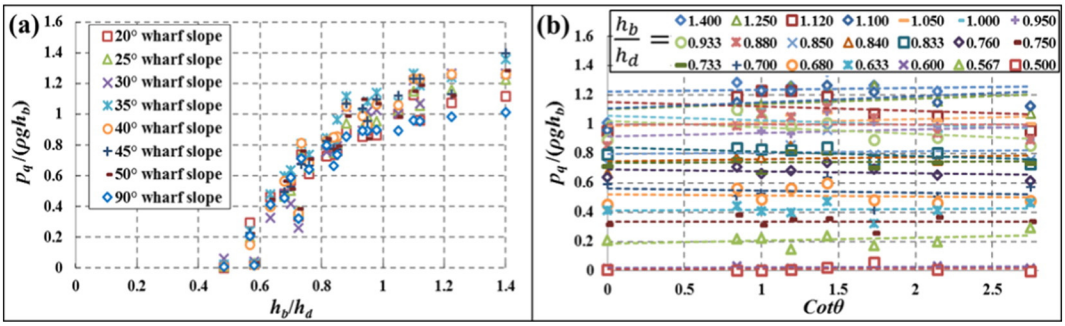

Fig. 15. Relationship between normalized quasi-steady pressure and the parameters in Eq. (4).

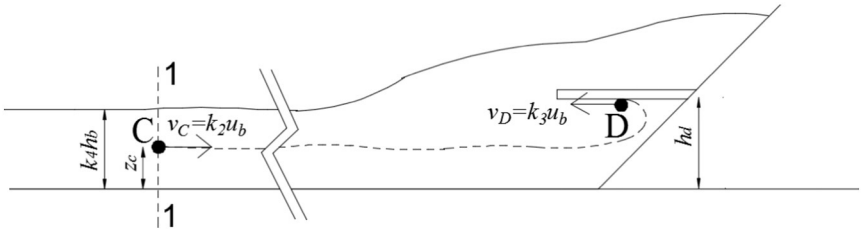

Fig. 16. Flow characteristics in the quasi-steady stage.

where h_{max} is the maximum height that bore front can reach; u_A and u_B are velocities of the unit water volume at positions A and B, respectively; $0.5k_1\rho v_A^2$ is the energy loss term arising from friction and other external forces acting while the unit volume travels from A to B, and k_1 is the energy loss coefficient.

Because $v_A = u_b$, $v_B = 0$, Eq. (9) can be deduced from Eq. (8):

$$\frac{h_{max}}{h_b} = \frac{1}{2}(1-k_1)\frac{u_b^2}{gh_b} + 1 \tag{9}$$

Combining Eqs. (1) and (9) gives:

$$\frac{h_{max}}{h_b} = \frac{1}{2}Fr_b^2(1-k_1) + 1 \tag{10}$$

The critical condition that $p_f/(\rho g h_b) = 0$ is when $h_d = h_{max}$, because the bore front cannot climb high enough to hit the soffit of the deck. So the critical condition for $p_f = 0$ is:

$$\frac{h_d}{h_b} = \frac{1}{2}Fr_b^2(1-k_1) + 1 = C_1 \tag{11}$$

For the average value of $Fr_b = 1.6$ in this study, $C_1 = 2.28 - 1.28k_1$. If there is no energy change during bore climbing up on the slope ($k_1 = 0$), $C_1 = 2.28$; the value of C_1 from the experimental data is 2.0, giving energy loss coefficient in this study, $k_1 = 0.22$.

Combining Eqs. (7) and (11), the normalized front-hitting pressure is:

$$\frac{p_f}{\rho g h_b} = (\cot\theta + C_2) * \ln\left[\frac{h_b}{h_d} * \left(\frac{1}{2}Fr_b^2 + 1 - \frac{1}{2}k_1Fr_b^2\right)\right]$$

$$for\ 0.5 \le \frac{h_b}{h_d} \le 1.4,\ 20^\circ \le \theta \le 90^\circ,\ Fr_b = 1.6 \tag{12}$$

where $C_2 = 1.83$ by fitting from the experiment data.

Fig. 14 compares measured pressure values and values calculated using Eq. (12). In general, the equation error is <20%.

4.2.3. Equation for estimating quasi-steady pressures

Fig. 15(a) and (b) show the relationships between the normalized quasi-steady pressure and the height and wharf slope parameters in Eq. (4), respectively. The normalized quasi-steady pressure increases with increasing h_b, and decreases with increasing h_d, but the data are scattered. However, as seen from Fig. 15(a), a correlation exists between the normalized quasi-steady pressure and the dimensionless parameter (h_b/h_d). As seen from Fig. 15(b), for each value of (h_b/h_d), the normalized quasi-steady pressure has an approximately constant value, showing that the wharf slope angle has little effect on the quasi-steady pressure.

Considering the basic theory (Fig. 16), in the quasi-steady stage, there must be a unit water volume C in the section 1–1 that is in the same streamline as a unit water volume D under the deck soffit. Thus Bernoulli's equation can applied:

$$\frac{p_C}{\rho g} + z_C + \frac{v_C^2}{2g} = \frac{p_D}{\rho g} + z_D + \frac{v_D^2}{2g} \tag{13}$$

where p_C and p_D are the pressures at C and D, respectively; z_C and z_D are the elevations of C and D, respectively ($z_D = h_d$); v_C and v_D are the velocities of unit water volumes at C and D, respectively.

In the quasi-steady stage, $p_D = p_q$, where p_q is the maximum deck-averaged quasi-steady pressure. The flow is assumed to be steady, thus the velocities at C and D do not change during this stage. Therefore,

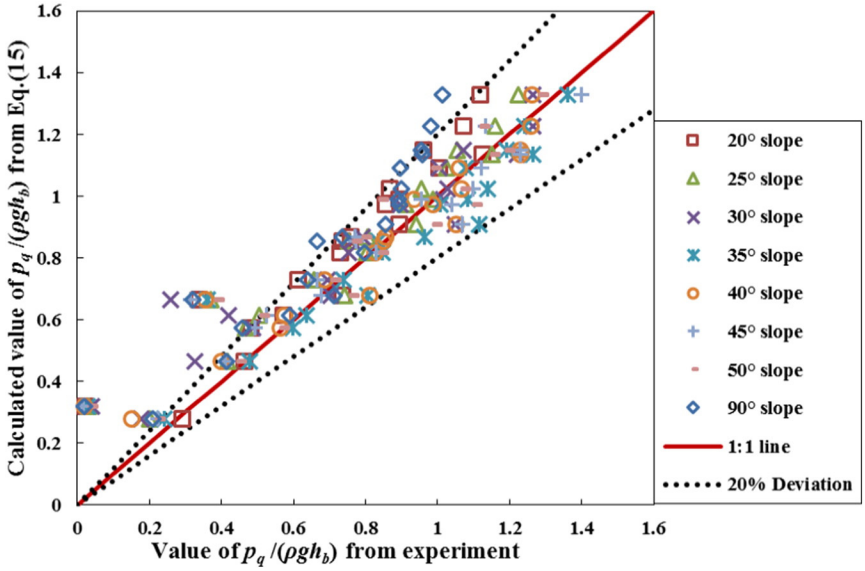

Fig. 17. Comparison of values of normalized quasi-steady pressure from Eq. (15) and from experiment.

$v_C = k_2 u_b$, $v_D = k_3 u_b$, and the water level in section 1–1 is $k_4 h_b$, where k_2, k_3, k_4 are constant coefficients in each test. Assuming uniform flow in section 1–1, $p_C = \rho g(k_4 h_b - z_C)$.

So the following equation can be obtained from Eq. (13):

$$k_4 h_b + \frac{k_2^2}{2}\frac{u_b^2}{g} = \frac{p_q}{\rho g} + h_d + \frac{k_3^2}{2}\frac{u_b^2}{g} \tag{14}$$

Combining Eqs. (1) and (14) gives the quasi-steady pressure equation as:

$$\frac{p_q}{\rho g h_b} = C_3 - \frac{h_d}{h_b} \; for \; 0.5 \le \frac{h_b}{h_d} \le 1.4, 20^\circ \le \theta \le 90^\circ, Fr_b = 1.6 \tag{15}$$

where $C_3 = k_4 + 0.5(k_2^2 - k_3^2)Fr_b^2$. Assuming that the pressure is hydrostatic, $k_2 = k_4 = 1$ and $k_3 = 0$, yielding $C_3 = 1 + 0.5Fr_b^2 = 2.28$ (for $Fr_b = 1.6$). In this study, the experimental value of C_3 is 2.04, which is 10.5% less than the value of C_3 from the assumption of hydrostatic pressure.

Fig. 17 compares measured pressure values and values calculated using Eq. (15). In general, the equation error is <20%.

5. Conclusions

In this study, tsunami bore uplift loads on a wharf model were quantified. The bore characteristics were investigated. Also, the bore height, deck height and slope angle effect on uplift loads were investigated. The main conclusions are summarised below:

1) In our study, the flow motion around the wharf model exhibits five stages, namely front-climbing stage, front-hitting stage, run-up stage, quasi-steady stage, and recession stage. Correspondingly, the time-history of pressure exhibits front-climbing pressure (small fluctuation signals), front-hitting pressure (the largest peak), run-up pressure (large fluctuations), quasi-steady pressure (the longest time), and recession pressure (dropping to zero).
2) In the front-hitting stage, the pressure is dominated by dynamic pressure, and the variations of pressure profile along the deck stream-wise centreline occur in this stage. In the quasi-steady stage, the pressure is dominated by hydrostatic pressure, and the pressures are evenly distributed along the stream-wise centreline of the deck. Both front-hitting pressure and quasi-steady pressure reduce from the deck-slope connection to the deck front edge, and are constant in the transverse direction.
3) Both front-hitting pressure and quasi-steady pressure increase as bore height increases or deck height decreases. A smaller wharf slope angle results in a higher front-hitting pressure, but there is little effect of slope angle on quasi-steady pressure. For the 90° wharf slope, a front-hitting pressure was not observed on most of the deck but was observed at the deck-slope joint.
4) From our experimental results, uplift pressure is found to be a function of bore height, deck height and wharf slope angle. The equations for estimating averaged front-hitting pressure and quasi-steady pressure are proposed as Eqs. (12) and (15), respectively. The uplift pressures calculated by the equations agree with the measured pressure within ±20% error.

Acknowledgements

The first author would like to thank China Scholarship Council (CSC) (201406710035) for the financial support of this research. Funding from the Natural Hazards Research Platform, New Zealand (2012-GNS-03-NHRP), is gratefully acknowledged. Also, the valuable suggestions from Dr. Keith Adams and two anonymous reviewers are appreciated.

Appendix A. Supplementary data

Supplementary data to this article can be found online at http://dx.doi.org/10.1016/j.coastaleng.2016.08.001.

References

Al-Faesly, T., Palermo, D., Nistor, I., Cornett, A., 2012. Experimental modeling of extreme hydrodynamic forces on structural models. Int. J. Protect. Struct. 3 (4), 477–506. http://dx.doi.org/10.1260/2041-4196.3.4.477.
Araki, S., 2015. Pressure acting on underside of bridge deck. Procedia Eng. 116, 454–461. http://dx.doi.org/10.1016/j.proeng.2015.08.313.
Araki, S., Deguchi, I., 2012. Prediction of wave force acting on horizontal plate. Coast. Eng. Proc. 1 (33), 52 (https://icce-ojs-tamu.tdl.org/icce/index.php/icce/article/viewFile/6998/pdf_1).
Araki, S., Ishino, K., Deguchi, I., 2011. Stability of girder bridge against tsunami fluid force. Coastal Engineering Proceedings, 1(32): Structures. 56 (https://icce-ojs-tamu.tdl.org/icce/index.php/icce/article/viewArticle/1413).
Bryant, E., 2008. Tsunami: the Underrated Hazard. Springer.
CCH, 2000. City and County of Honolulu Building Code (Chaper 16, Artical 11). 2000. Department of Planning and Permitting, Honolulu, Hawaii.
Chanson, H., 2005. Analytical solution of dam break wave with flow resistance: application to tsunami surges. 31st IAHR Biennial Congress, pp. 3341–3353 (http://espace.library.uq.edu.au/view/UQ:9186/iahr0506.pdf).
Chanson, H., 2006. Tsunami surges on dry coastal plains: application of dam break wave equations. Coast. Eng. J. 48 (4), 355–370. http://dx.doi.org/10.1142/S0578563406001477.
Chanson, H., 2009. Application of the method of characteristics to the dam break wave problem. J. Hydraul. Res. 47 (1), 41–49. http://dx.doi.org/10.3826/jhr.2009.2865.
Chock, G., Robertson, I., Riggs, H.R., 2011. Tsunami structural design provisions for a new update of building codes and performance-based engineering. Proceedings, Solutions to Coastal Disasters. 2011, pp. 423–435. http://dx.doi.org/10.1061/41185(417)38.
Contreras-Lopez, M., et al., 2016. Field survey of the 2015 Chile tsunami with emphasis on coastal wetland and conservation areas. Pure Appl. Geophys. 173 (2), 349–367. http://dx.doi.org/10.1007/s00024-015-1235-2.
Cuomo, G., Shimosako, K., Takahashi, S., 2009. Wave-in-deck loads on coastal bridges and the role of air. Coast. Eng. 56 (8), 793–809. http://dx.doi.org/10.1016/j.coastaleng.2009.01.005.
Cuomo, G., Tirindelli, M., Allsop, W., 2007. Wave-in-deck loads on exposed jetties. Coast. Eng. 54 (9), 657–679. http://dx.doi.org/10.1016/j.coastaleng.2007.01.010.
FEMA, 2012. Guidelines for Design of Structures for Vertical Evacuation from Tsunamis (FEMA P646). Federal Emergency Management Agency, Washington, USA (http://www.fema.gov/media-library-data/1426211456953-f02dffee4679d659f62f414639afa806/FEMAP-646_508.pdf).
Fritz, H.M., et al., 2011. Field survey of the 27 February 2010 Chile tsunami. Pure Appl. Geophys. 168 (11), 1989–2010. http://dx.doi.org/10.1007/s00024-011-0283-5.
Ghobarah, A., Saatcioglu, M., Nistor, I., 2006. The impact of the 26 December 2004 earthquake and tsunami on structures and infrastructure. Eng. Struct. 28 (2), 312–326. http://dx.doi.org/10.1016/j.engstruct.2005.09.028.
Grilli, S.T., et al., 2007. Source constraints and model simulation of the December 26, 2004, Indian Ocean tsunami. J. Waterw. Port Coast. Ocean Eng. 133 (6), 414–428. http://dx.doi.org/10.1061/(ASCE)0733-950X(2007)133:6(414).
Iizuka, H., Matsutomi, H., 2000. Damage due to flood flow of tsunami. Proceedings of the Coastal Engineering of JSCE. 47, pp. 381–385.
Kihara, N., et al., 2015. Large-scale experiments on tsunami-induced pressure on a vertical tide wall. Coast. Eng. 99, 46–63. http://dx.doi.org/10.1016/j.coastaleng.2015.02.009.
Kirkoz, M., 1983. Breaking and run-up of long waves, tsunamis: their science and engineering. Proceedings of the 10th IUGG International Tsunami Symposium.
Kosa, K., Nii, S., Miyahara, K., Shoji, M., 2010. Experimental study for estimating tsunami forces acting on bridge girders. Proc., 26th US–Japan Bridge Engineering Workshop, pp. 1–14 (http://pwweb1.pwri.go.jp/eng/ujnr/tc/g/pdf/26/26-5-4_kosa.pdf).
Lukkunaprasit, P., Ruangrassamee, A., 2008. Building damage in Thailand in the 2004 Indian Ocean tsunami and clues for tsunami-resistant design. IES J. A Civ. Struct. Eng. 1 (1), 17–30. http://dx.doi.org/10.1080/19373260701620162.
Lukkunaprasit, P., Ruangrassamee, A., Thanasisathit, N., 2009. Tsunami loading on buildings with openings. Sci. Tsunami Haz. 28 (5), 303 (http://76.163.202.61/285LUKKUNSPASIT.pdf).
Matsutomi, H., Sakakiyama, T., Nugroho, S., Matsuyama, M., 2006. Aspects of inundated flow due to the 2004 Indian Ocean tsunami. Coast. Eng. J. 48 (02), 167–195. http://dx.doi.org/10.1142/S0578563406001350.
Murty, T.S., 1977. Seismic Sea Waves: Tsunamis, Bulletin 198. Department of Fisheries and the Environment, Fisheries and Marine Service, Ottowa, Canada.
Nandasena, N., Sasaki, Y., Tanaka, N., 2012. Modeling field observations of the 2011 great east Japan tsunami: efficacy of artificial and natural structures on tsunami mitigation. Coast. Eng. 67, 1–13. http://dx.doi.org/10.1016/j.coastaleng.2012.03.009.
Nandasena, N., Tanaka, N., 2013. Boulder transport by high energy: numerical model-fitting experimental observations. Ocean Eng. 57, 163–179. http://dx.doi.org/10.1016/j.oceaneng.2012.09.012.
Nouri, Y., Nistor, I., Palermo, D., Cornett, A., 2010. Experimental investigation of tsunami impact on free standing structures. Coast. Eng. J. 52 (01), 43–70. http://dx.doi.org/10.1142/S0578563410002117.
Rahman, S., Akib, S., Shirazi, S., 2014. Experimental investigation on the stability of bride girder against tsunami forces. Sci. China Technol. Sci. 57 (10), 2028–2036. http://dx.doi.org/10.1007/s11431-014-5628-8.

Robertson, I., Paczkowski, K., Riggs, H., Mohamed, A., 2013. Experimental investigation of tsunami bore forces on vertical walls. J. Offshore Mech. Arct. Eng. 135 (2), 021601. http://dx.doi.org/10.1115/1.4023149.

Robertson, I., Riggs, H., Mohamed, A., 2008. Experimental results of tsunami bore forces on structures. ASME 2008 27th International Conference on Offshore Mechanics and Arctic Engineering, pp. 509–517 http://dx.doi.org/10.1115/OMAE2008-57525.

Suppasri, A., et al., 2012. Damage characteristic and field survey of the 2011 great east Japan tsunami in miyagi prefecture. Coast. Eng. J. 54 (01), 1250005. http://dx.doi.org/10.1142/S0578563412500052.

Yeh, H., Sato, S., Tajima, Y., 2013. The 11 March 2011 east Japan earthquake and tsunami: tsunami effects on coastal infrastructure and buildings. Pure Appl. Geophys. 170 (6–8), 1019–1031. http://dx.doi.org/10.1007/s00024-012-0489-1.

Yeh, H.H., Ghazali, A., Marton, I., 1989. Experimental study of bore run-up. J. Fluid Mech. 206, 563–578. http://dx.doi.org/10.1017/S0022112089002417.